Fracture Behavior of Crop Circle Ceramic Tiles: Experimental and Numerical Study

Ay Lie Han[1], Bobby Rio Indriyantho[1,*], Mhd Rony Asshidiqie[2], Purwanto[1], Widowati[3], Kartono[3], I Nyoman Jujur[4]

[1]Department of Civil Engineering, Universitas Diponegoro, Semarang, Indonesia

[2]Department of Civil and Disaster Prevention Engineering, National United University, Miaoli, Taiwan

[3]Department of Mathematics, Universitas Diponegoro, Semarang, Indonesia

[4]Advanced Material Research Center, National Research and Innovation Agency, Jakarta, Indonesia

Received 08 November 2023; received in revised form 03 January 2024; accepted 04 January 2024

DOI: https://doi.org/10.46604/ijeti.2024.13070

Abstract

This research investigates the effect of three-dimensional (3D) bee-crop-circle tiles on load deformation, initial cracking and propagation, and stress redistribution. Experimental tests provide limited data due to the small specimen size and brittle nature of the material. A finite element (FE) model is constructed and validated by laboratory data to analyze the stress-strain responses and failure mode. The model enables a detailed description of stress patterns, stress propagation, and redistribution of layers beneath the bee design. The study concludes that a 3D crop circle-inspired design significantly influences the ultimate load-carrying capacity and stress-related behavior. The load-deformation response is nonlinear, and the coloring influences the thickness of coatings, further affecting the ultimate load and initial stiffness. Furthermore, designs with convex details result in an arc action, deviating the stress concentrations away from the line of loading. The FE model slightly overestimates the initial stiffness but represents the ultimate load and load-displacement response with high accuracy.

Keywords: ceramics, crop circle tiles, mechanical and physical properties, fracture behavior, finite element model

1. Introduction

Since modern technology has evolutionarily transcended inherent parts of nature, natural, physical, and biological phenomena can be simulated through computer programming. From a scientific perspective, natural phenomena are perceived to be irregular, intricate, and sometimes incomprehensible. Consequently, to draw a solution, non-deterministic patterns are introduced owing to the interpretability by computer science based on iterative dynamics. Specifically, crop circles are among one of the most intriguing visual configurations. Modern generative visualization initiates the acquisition of computer technology by creating iterative visualization rules and transforms the complicated forms into ten basic simple forms. Concerning crop circles, undoubtedly, this basic form is a circle. Moreover, crop circles can be interpreted as aesthetic objects with a pseudo-algorithmic configuration [1-2].

The Berbah-Sleman crop circles in Central Java were formed in rice fields and are the inspiration for the tile design investigated in this study [3]. The study identified the geometric variables of the circles: the center, radii, and intersection coordinates, and the data were generated in a computer program, resulting in an algorithm representing the geometric pattern of

* Corresponding author. E-mail address: bobbyrio@live.undip.ac.id

English language proofreader: Chih-Wei Chang

crop circles. Inspired by the mathematical formulation of these crop circles, a design for hand-painted tiles was developed (Fig. 1(a)). The design started with the creation of basic configurations, which were subsequently developed into generative motifs, such as symmetrical batik (a specific fabric design originating in Indonesia [4]) and decorative tiles, among others. Fig. 1(b) visibly shows the visual design of a bee pattern based on the crop circle analogy. The circles forming the bee are seen in this picture. Furthermore, the individual tiles can be manipulated to create new algorithms, samples of which are shown in Fig. 2.

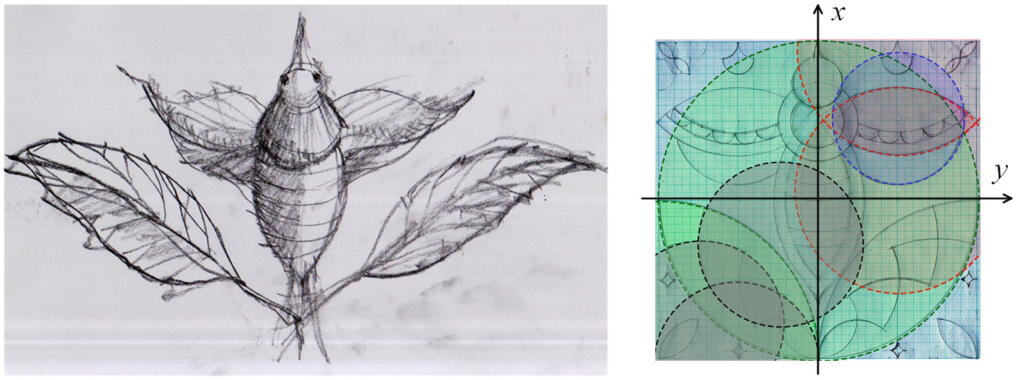

(a) Artistic presentation of bee design (b) Algorithm based on crop circle

Fig. 1 The design of the bee pattern

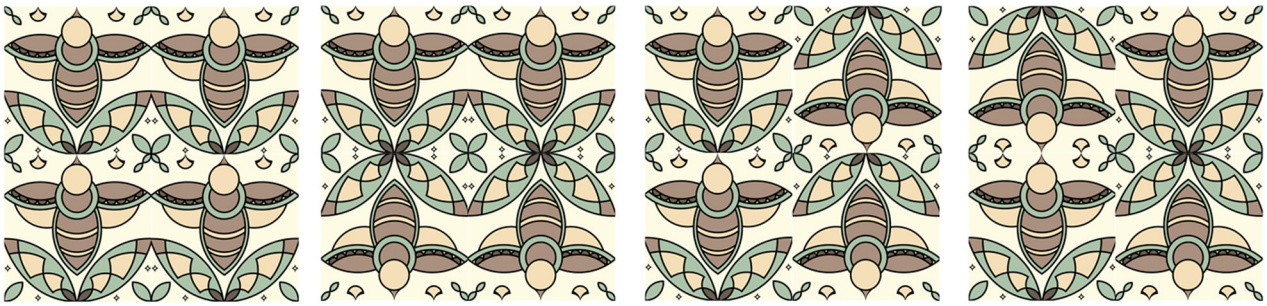

Fig. 2 Algorithm innovations

Regarding quality performance, the tiles should fulfill the minimum strength and ductility requirements. The curvature on and perpendicular to the tile plane with the thickness and configuration of the bees, affecting the initial stresses, cracking, stress propagation, and failure mechanism in the tile, all due to the design that created a three-dimensional (3D) image. Hence, experimental tests were conducted using a three-point flexural mechanism with a load-controlled increment.

This configuration created high bending stresses, in combination with pronounced shear stresses, which was the most critical loading condition. To distinguish the load configurations concerning the design, the Cartesian axes system was addressed, i.e., the *y*-axis is perpendicular to the bee's anatomy and the *x*-axis goes through the body (Fig. 1(b)). The final design resulted in two color variations, red and blue, expanding the numerations to R-x and R-y for sampling of the red-colored tiles with loading along the *x* and *y* direction, respectively. The numeration B referred to the blue-colored tiles. The absorption rate of the red and blue colored specimens was also sought to underline the mechanical properties.

To examine the strain and stress propagation thoroughly, a 3D finite element (FE) model was constructed using identical physical and mechanical properties of a tile. This model enabled biaxial stress analysis based on the failure envelope. The model also incorporated the material's constitutive stress-strain relationship. To ensure the meshing yielded in a load convergence, a sensitivity analysis was performed on the load increment followed by the actual experimental increment. Additionally, the unit weight was determined as an input to the model. The load displacement and crack pattern output of the FE model were validated by the experimental results before further analysis into stress concentrations and failure mode were carried out.

Previous research into the influence of sintering temperature and duration was conducted on a wide range of tile types [5-6]. First, Abiola et al. [7] determined the optimum processing temperature for clay-feldspar-silica tiles stands at 1300 ℃, resulting in flexural strength of 12-20 MPa, while Bernardo-Arugay et al. [8] used Philippines-based nickel laterite mine waste, concluding that the fluctuation in modulus of rupture followed a quadratic concave pattern with a bifurcation point at 1500 ℃ and flexural strength of 12-15 MPa. Second, Húlan et al. [9] studied the influence of fly ash on clay-based ceramics and underlined that fly ash negatively influenced the modulus of rupture and flexural strength. The addition of fly ash also reduced the bulk density and there was an interesting response of Young's modulus to the sintering temperature. Although a maximum was found at 1500 ℃, the pattern demonstrated a spike at around 300 ℃, after which a reduction was seen, followed by an increase (to a maximum of 1000 ℃). Then, Thakur et al. [10] exclusively investigated the effect of sintering temperature on cupola furnace slag, yielding a temperature of 1000-1100 ℃ as a maximum, resulting in a flexural strength of 24-28 MPa.

Numerous works have been dedicated to the development of methods and equipment to detect surface defects [11-15]. The impact of sound waves was used by Zhao [13], while Zhang et al. [12] and Lu et al. [14] accessed a light source, with a high-resolution camera. The designed apparatus was connected to a conveyor belt for continuous testing. Deep learning was proposed by Wan et al. [15], constructing a model based on the YOLOv3 and single shot multibox detector (SSD) models. A review of available methods can be found in Schabowicz [11].

Generally, flexural strength behavior has been of the utmost interest and has been studied extensively [7, 9, 16]. Most loading configurations concerned the three-point loading system [7, 9, 17-19]. A wide range of flexural strengths were determined, mainly a function of the basic materials, addition of components, sintering temperature and duration, and porosity. The surface conditions significantly influenced the flexural strength [16, 20].

Based on the state-of-the-art wall tiles' behavior analyses, the tiles herein were sintered at a temperature of 1000 ℃ and then coated and reheated to 1500 ℃, which is the optimum sintering temperature. The resulting modulus of rupture, however, was slightly lower than the recorded results. It can be attributed to the use of a traditional furnace and the temperature increase rate during sintering. Another factor was the basic material, which differed from the material used by the previous researchers. The decision on the three-point loading system was, besides the guidelines of the code, also inspired by the methods previously used in experimental testing. Very limited data is available on the influence of 3D design on the mechanical behavior of tiles. The 3D design influences the response to loading. Stress concentration arises in the material as a direct relationship to its relief, and initial cracking is affected by the design. Information on the responses of 3D tile design on these mechanical aspects is important for further design criteria and optimization. This study explains the rationale behind the effect of the crop circle design on the strength of the tiles and defines the determination of the mechanical and physical properties of this unique type of tile, their design influence on the strength, and the failure behavior.

2. Research Significance

Unlike floor tiles, wall tiles can generate complex 3D designs. The crop circle tiles considered hereof were indoor wall tiles, and predominantly severe weather impacts, such as direct sunlight, rain, hail, or snow, were not considered in the study. The design of the reliefs influences the load-carrying capacity, the mode of failure, and the overall behavior of the element under loading. Furthermore, coloring also affects the mechanical behavior of these tiles. The 3D reliefs and differentiations in thickness throughout the tile result in a significant impact on the stress distribution and crack initiation and propagation due to stress concentrations. The orientation of loading, concerning the axes, also determines the stress response of these tiles. Experimentally tested specimens could quantitatively constrain the anticipated information. Due to their brittle nature, the failure would abruptly incur and consequently result in the loss of expected accuracy on visual observations. This qualitative observation cannot yield detailed data on the stress propagation and mode of failure due to incremental loading.

One method to enable the in-depth analysis of such an element is through the construction of realistic 3D models. The boundary conditions, supports, and loading sequences should represent the actual test set-up with great accuracy. A valid model provides the researcher with a wide range of information which, in turn, can be used as an optimization guideline for the designer. 3D designs should be analyzed numerically at first, to avoid mechanically infeasible reliefs. The model can be used to adjust or optimize a design so that the visual appearances and the capacity of the tile, as an element, match the criteria. This research work demonstrates the essence of modeling to analyze stress and strain behavior thoroughly, and this method could be incorporated further into standards or codes. The effect of colors should also be determined before decision-making since coloring significantly influences the mechanical response of 3D tiles.

3. Material and Methods

The research was conducted experimentally, by testing bee-crop-circle tiles in the laboratory, and numerically, by constructing an FE model with the identical physical and mechanical properties as the experimentally tested specimens. The load configurations, boundary conditions, increment rates, and additional relevant information were simulated in the model. The load-displacement relationships obtained from the laboratory-based specimens were used as a validation tool for the FE model. The model was further employed to explain the influence of 3D design on the behavior of the tiles.

The test specimens were 3D crop circle wall tiles with a color variation of blue and red (Fig. 3). The dimension L and the thickness t were obtained as 100.38 × 10.17 mm for the red tiles and 100.52 × 10.33 mm for the blue ones, based on the international organization for standardization (ISO) 10545-2:2018 Ceramic Tiles - Part 2 (Determination of dimensions and surface quality). The thickness was defined at the reliefs with the code. Since the tiles were hand-painted, each tile had unique characteristics, and these measurements were analytically accessed in the calculations and modeling.

Etymologically, the word “ceramics” is derived from the Greek word *Keramos*, reflecting burned clay. The clay used for these tiles was stoneware [5, 21-23], which was adequately graded. The tiles were cast and dried under room conditions for 3-5 days and burned at 900-1000 °C for 24 hours. After cooling, the tiles were hand-painted, and the paint functioned as glazing and coating. The tiles were re-heated up to 1250 °C for another 24 hours, resulting in the shiny appearance seen in Fig. 3. Previous studies found that the temperature and duration of sintering significantly influenced the strength [7-8]; the temperature chosen fell within these research results.

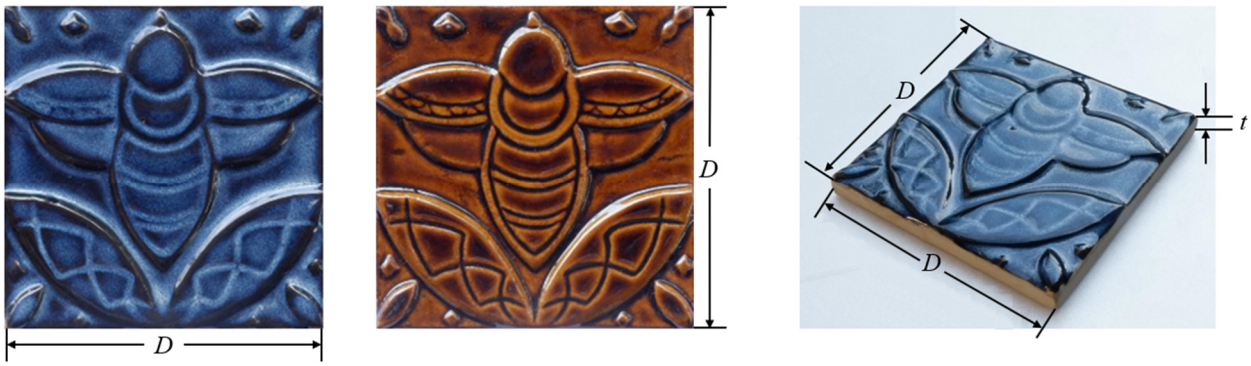

Fig. 3 Specimen and color variation of ceramic specimens

The bulk density and absorption were obtained, based on ISO 10545-3:2018 Ceramic Tiles - Part 3 (Determination of water absorption, apparent porosity, apparent relative density, and bulk density). The bulk density was also tested, using the mercury submersion method [24]. The blue specimens had a density of 2.15 gr/cm^3, with an absorption rate of 0.9%; the red tiles had a density of 2.17 gr/cm^3 and an absorption rate of 0.6%. The red tiles were somehow influenced negatively by the dye, compared to the blue ones.

3.1. Experimental study

The tiles were tested to obtain the mechanical properties of the specimens (Fig. 4). The supports were located 80 mm apart and the load was situated at the center, as seen in Fig. 5(a). The specimens were tested using a three-point loading system, as seen in Fig. 4(a). The test was load-controlled at increments of 0.01 MPa/second. The loads and displacements were recorded by a load cell and a linear variable differential transformer (LVDT), respectively. As presented in Fig. 5(b) and 5(c), two loading conditions were considered: along the line of the bee's body (in the *x*-axis direction) and perpendicular to this direction (the *y*-axis). This loading variation was purposively introduced to determine the influence of 3D crop design on the load-carrying capacity. Both rubber bearing pads placed under the loading rod and at the supports had a thickness of 5±1 mm. One support was constrained in all translation and rotation directions, while the support with a spring was constrained against translation but allowed a rotational degree of freedom. The test set-up was based on ISO 10545-4:2019 Ceramic Tiles - Part 4 (Determination of modulus of rupture and breaking strength standards).

This loading configuration combined high flexure and shear stresses in the line of loading. Since the material is weak in tension, the initial cracking occurs in this area, at the outer bottom fibers in tension. The load was applied on the glazed surface, simulating the actual condition of the wall tile. This loading mechanism is widely used and results in accurate predictions of flexural strength.

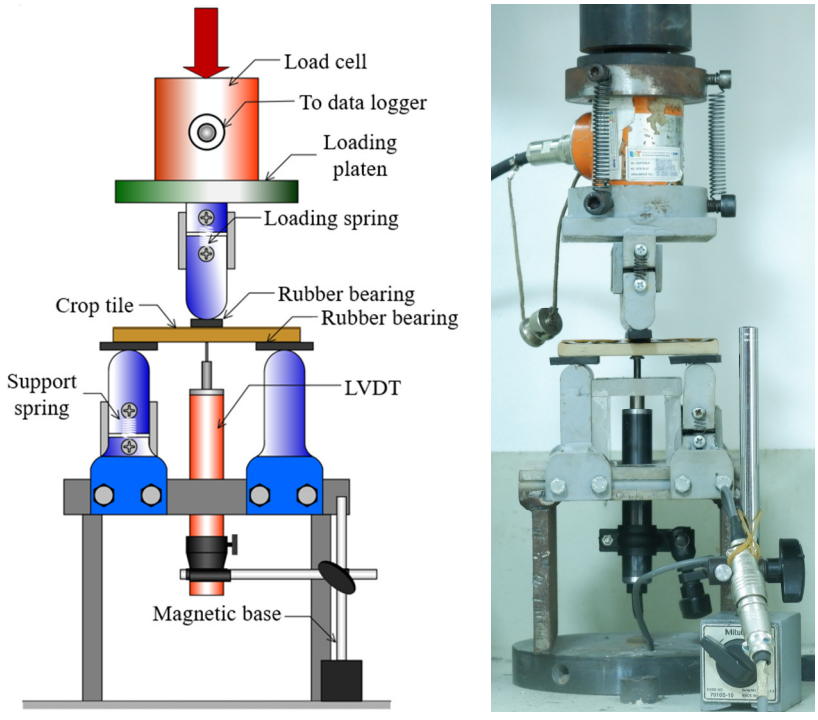

(a) Diagram of the testing method (b) Laboratory testing

Fig. 4 Test set-up

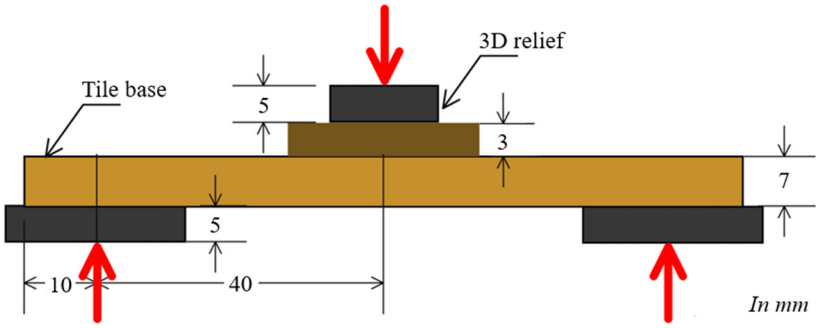

(a) Loading scheme

Fig. 5 Loading scheme and boundary conditions

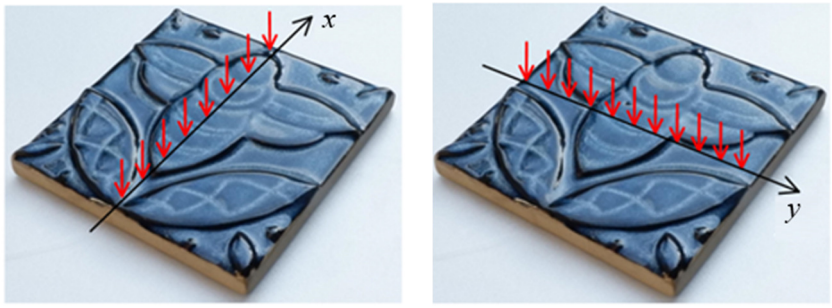

(b) Loading in the *x*-axis direction (c) Loading in the *y*-axis direction

Fig. 5 Loading scheme and boundary conditions (continued)

3.2. *Finite element modeling*

A 3D model of the crop circle tile was constructed. The software LS DYNA v.4.6.17 was employed for FE analysis, providing a robust computational framework. The main objective was to comprehend how static loading influences stress distribution in these 3D patterned ceramic tiles and to evaluate the effect of the revolved loading axis on stress behavior. The FE model was validated for the load-displacement behavior from the experiment.

Explicit analysis was used herein with the following assumptions: ceramic is an isotropic material modeled without pores, while the loading condition is steady with a low loading rate and ideally supported (as mentioned in the guidelines) and the support behaves as a rigid material. This assumption was made owing to the great uncertainty in the experimental specimens and setup, which can influence the validation of FE results. Thus, the subsequent sections elaborate on the geometry, constitutive materials, element types, and boundary conditions of this analysis.

3.2.1. *Geometry*

Referring to the geometric data, the ceramic was designed with a thickness of 10 mm at the reliefs and 7 mm at the base of the tiles. The horizontal dimensions were taken to be 100 × 100 mm. The pattern of the bees followed circles on intersecting lines, with each circle having the coordinates and radii presented in Fig. 6(a) and Table 1. The numeration reflects the data of the circle's central coordinates and radii length. Identical to the experimental tests, the supports, loading configurations, and the meshing of the FE model, are displayed in Fig. 6(b).

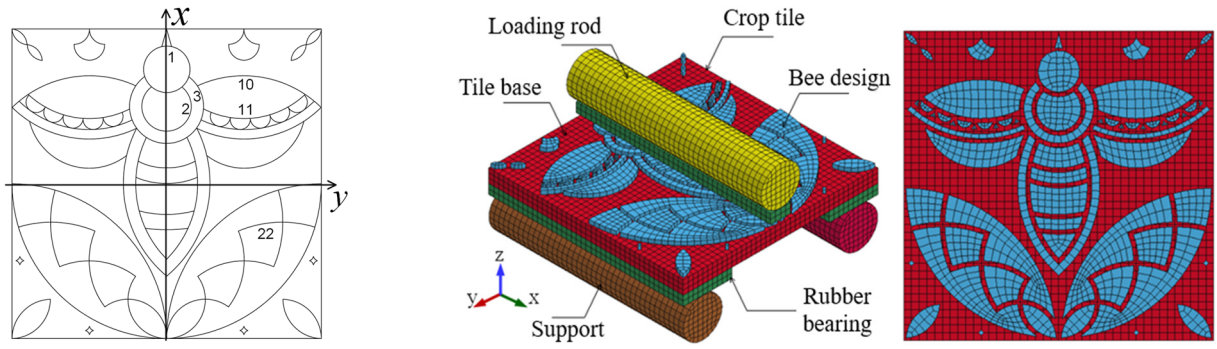

(a) Coordinates of intersections and circle radii (b) FE model

Fig. 6 Modeling of bee-crop-circle tiles

Table 1 Bee pattern circle center and radii coordinate sample, as in Fig. 6(a)

Line code	Coordinate of circle center (*x*, *y*)	Radius length (mm)	Line code	Coordinate of circle center (*x*, *y*)	Radius length (mm)
1	(0,37)	7.5	10	(25,0)	35.0
2	(0,25)	8.0	11	(25,50)	29.0
3	(0,25)	12.0	22	(27.5,-50.0)	37.5

3.2.2. Ceramic model

To simulate the brittle nature of the ceramic's properties, the Johnson-Holmquist 2 (JH-2) material model was deployed [25]. The JH-2 model enables the capturing of the elastic-brittle behavior at the initial loading stages and the post-yield response before load termination, providing the most satisfactory parameters for simulating the material brittleness and fracture failure. The following formula describes the material's behavior; the material's strength is determined by a dynamic function σ^*, considering the intact strength σ_i^*, fractured strength σ_f^*, and damage D.

$$\sigma^* = \sigma_i^* - D\left(\sigma_i^* - \sigma_f^*\right) \tag{1}$$

The strength parameter was adjusted based on the Hugoniot elastic limit (HEL), to simplify the comparison of different materials. The stress affecting HEL, σ_{HEL}, is described in:

$$\sigma_{HEL} = \frac{2}{3}\left(HEL - P_{HEL}\right) \tag{2}$$

where P_{HEL} is the pressure at the HEL. The normalized intact and fracture strength as defined in:

$$\sigma_i^* = A\left(P^* + T^*\right)^N \left(1 + C\ln\dot{\epsilon}^*\right) \tag{3}$$

$$\sigma_f^* = B\left(P^*\right)^M \left(1 + C\ln\dot{\epsilon}^*\right) \tag{4}$$

where the normalized pressure P^*, and the normalized maximum tensile hydrostatic pressure T^* that the material can handle were adjusted based on P_{HEL}, while A, B, C, M, and N are compression parameters. The focus of this simulation was on the flexural stresses, accentuating the tensile strength over compression strength because of the tensive weakness of the material. The weakness in tension yields a sudden and brittle failure. Consequently, the parameters associated with compression behavior, specifically the B, C, and M parameters, are negligible [26]. Meanwhile, the damage variable D of JH-2 can be expressed by,

$$D = \sum \frac{\Delta\epsilon_p}{\epsilon_p^f} \tag{5}$$

where $\Delta\epsilon_p$ represents the increase in plastic strain, and ϵ_p^f denotes the plastic strain at fracture, based on the current pressure, as expressed in,

$$\epsilon_p^f = D_1\left(P^* + T^*\right)^{D_2} \tag{6}$$

The material deformation μ and pressure deformation P are calculated by:

$$\mu = \frac{\rho}{\rho_0} - 1 \tag{7}$$

$$P = K_1\mu + K_2\mu^2 + K_3\mu + \Delta P \tag{8}$$

where ρ and ρ_0 denote the current and initial density, respectively. Moreover, K_1, K_2, and K_3 are the material constants, while ΔP is additional incremental pressure. However, the flexural nature of the specimen would reduce the pressure P as in:

$$P = K_1\mu \tag{9}$$

with $K_1 = K$ as the bulk modulus.

Due to the linear equation of state, the expression for P_{HEL} can be formulated using HEL, along with two elastic moduli: the bulk modulus K and the shear modulus G, taken as 16.08 GPa and 11.57 GPa, respectively. These parameters were derived from Hooke's law, postulating a constant elastic modulus E of 28 GPa and a Poisson's ratio v of 0.21. Consequently, P_{HEL} is removable from the group of unknown parameters, employing the subsequent equation [27]. The density was obtained as an average of the blue and red tiles, taken as 2.16 gr/cm^3.

$$P_{HEL} = HEL\left(1-\frac{4G}{3K+4G}\right) \tag{10}$$

The basic E parameter in this simulation was adopted due to the ceramic porosity, where a porosity of 1.6% corresponds to an elastic modulus of 28 GPa [28]. The unknown value parameters of JH-2 were taken from the references as base calculations [26, 29]. In this context, the strain failure criteria were adopted as element deletion whenever the specimen started to reach the value of the determined strain value FS. The summary of JH-2 parameters is enumerated in Table 2.

Table 2 JH-2 ceramic strength parameters

Parameters	Value
Intact normalized strength (A)	0.93
Intact strength pressure exponent (N)	0.6
Reference strain rate ($EPSI$)	1
Maximum tensile strength (T)	0.009 GPa
Hugoniot elastic limit (HEL)	4.6 GPa [29]
Pressure exponent at HEL (P_{HEL})	2.6 GPa [29]
Damage coefficient (D_1)	0.05 [26]
Damage coefficient (D_2)	1.00 [26]
Failure strain (FS)	0.005

3.2.3. Rubber bearing model

The rubber material was characterized as a hyperelastic incompressible material. The selection of Mooney-Rivlin as a hyperelastic material is based on its role as a load transfer medium while disregarding factors such as significant deformation and viscoelasticity within the elastomer. Considering these reasons, and the simplicity of determining the parameters, the efficiency of calculations in the Mooney-Rivlin equation also elicits the suitability for modeling elastomer materials hereof. The rubber was categorized as a medium-hard rubber, with 60 (international rubber hardness degree) IRHD. Using the first-order Mooney-Rivlin hyperelastic material, the strain energy of materials can be indicated as:

$$W(\lambda) = C_{01}\left(2\lambda+\frac{1}{\lambda^2}-3\right)+C_{10}\left(\lambda^2+\frac{2}{\lambda}-3\right) \tag{11}$$

with $\lambda = \lambda_1$ as

$$\lambda_1 = 1+\epsilon_{11} \tag{12}$$

where λ and λ_1 in Eq. (12) denote stretch and its principal, respectively, while ϵ_{11} defines the one-dimensional strain component of Green-St. Venant tensor **E**.

The physical parameter of 60 IRHD rubber was used, as stated in Jerrams and Bowen [30], where C_{01} = 0.0647 MPa, C_{10} = 0.916 MPa, v = 0.4995 and ρ = 750 kg/m^3 to accurately capture large deformations in rubber materials. The parameter C_{01} is sensitive, and, if changing its value, the parameter would change the global material stiffness of the system. The determination of C_{01} was performed depending on the hardness of the rubber, where it was taken as 60 IRHD or 28 GPa. According to Jerrams and Bowen [30], the value of C_{01} was adjusted to 0.417 MPa for the antecedent rubber. Moreover, the C_{01} coefficient is proportional to the stiffer the rubber material. Hence, when the specimen was tested, the rubber deformed slightly, resulting in a smaller displacement.

3.2.4. Element, boundary condition, and contact

The hexahedral 8-node element was favored for its distinct advantages in representing complex 3D geometries with higher accuracy. Within this modeling framework, two distinct hexahedral element types were employed. The first was the constant stress-reduced integration type, denoted as *SECTION_SOLID (ELFORM=1), designated for the representation of ceramic materials and rod support, to achieve fast computational results while maintaining accurate values due to the quasi-static conditions simulated. The second type is the fully integrated solid element denoted as *SECTION_SOLID (ELFORM=2), assigned specifically to the rubber material, allowing for more accurate shape transformation. In addition, controls were implemented to reduce the hourglassing effects caused by the hyperelasticity of the rubber.

The boundary conditions for loading and support align with the guidelines outlined in ISO-10545-4-2019. With the assumption that the rod comprised a rigid material, the boundary condition and the direction which was constrained could be set using the *MAT_RIGID keyword. Given this standard, the first support was constrained in all directions of translation and rotation, while the second support constrained the translation but allowed rotation around the axis, perpendicular to the cross-section of the rod. The same condition of secondary support was consistently applied to the loading rod, with the additional displacement-controlled load rate imposed specifically on the downward Z axis, which can be performed by inputting the *BOUNDARY_PRESCRIBED_MOTION_RIGID keyword in LS-DYNA. Fig. 7 explains the boundary condition of the ceramic simulation.

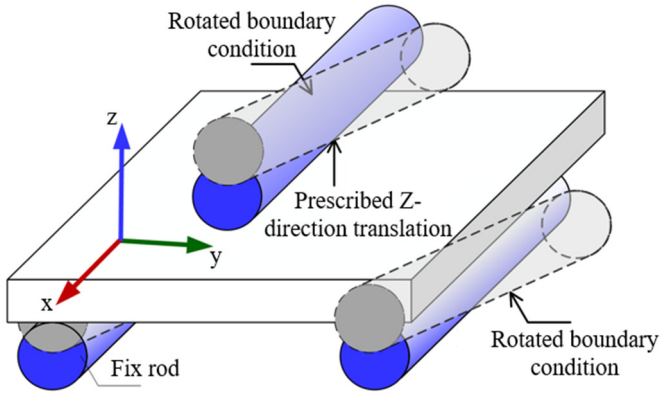

Fig. 7 Boundary condition of loading and support rod

The contact between the bee pattern and the ceramic is inseparable. The contact between the rubber, the ceramic, and the rod used the parameter of the static and dynamic coefficients of the Coulomb friction, of 0.2. In addition to the soft material, a SOFT constraint formulation was added to the surface contact within the rubber-tile and rubber-rod contact.

4. Results and Analysis

The load-displacement responses as the result of the experimental investigations, i.e., the modulus of rupture test and the breaking strength testing were then validated to the numerical simulations using LS DYNA. The data from both the red and blue tiles was scattered and compared to the response generated by the simulations. In addition to the load-displacement behavior, the failure pattern of the ceramic tiles was observed corresponding to the *x* and *y* axes. Furthermore, the stress distribution and the cracking of the tiles resulted from the software were also analyzed and discussed.

4.1. Experimental data

The load-displacement behavior is shown in Fig. 8(a) and 8(b). The pattern followed a quadratic convex path. Nonlinearity results from the clay's mechanical properties and micro-crack propagation between voids, yielding a stress redistribution after each crack formation. The cracks tend to propagate through the voids. The convex response was influenced by the presence of

rubber bearings. Under increasing stress, the rubber compacted, resulting in an enhanced material stiffness. The ultimate load-carrying capacity, displacement, initial stiffness, and modulus of rupture are shown in Table 3. The modulus of rupture was calculated with the equation from the code.

Table 3 List of mechanical properties obtained from the experimental test results

Notation	Ultimate load (N)	Ultimate displacement (mm)	Initial stiffness (N/mm)	Modulus of rupture (MPa)
R-x	820.09	1.30	122.57	9.48
R-y	789.37	1.61	87.86	9.12
B-x	957.75	1.47	185.45	10.71
B-y	827.10	1.41	175.08	9.25

The loading in the *x*-axis direction generally resulted in a higher ultimate load, compared to the *y*-axis direction (Fig. 8(c)). It is factually explicable that, along the *x*-axis, the relative thickness of the specimen is constantly higher than the base tile part, providing a larger moment of inertia. The base had a thickness of 7 mm, compared to 10 mm at the bee-reliefs. In this *x* direction, the red tiles had a 4% higher ultimate load carrying capacity, while that for blue tiles was 16% (Fig. 8(d)). In other words, the blue tiles had a slightly better performance. The blue paint resulted in a thicker coating, which is reflected by the differentiation of 10.17 mm for the red tiles versus 10.33 mm for the blue tiles.

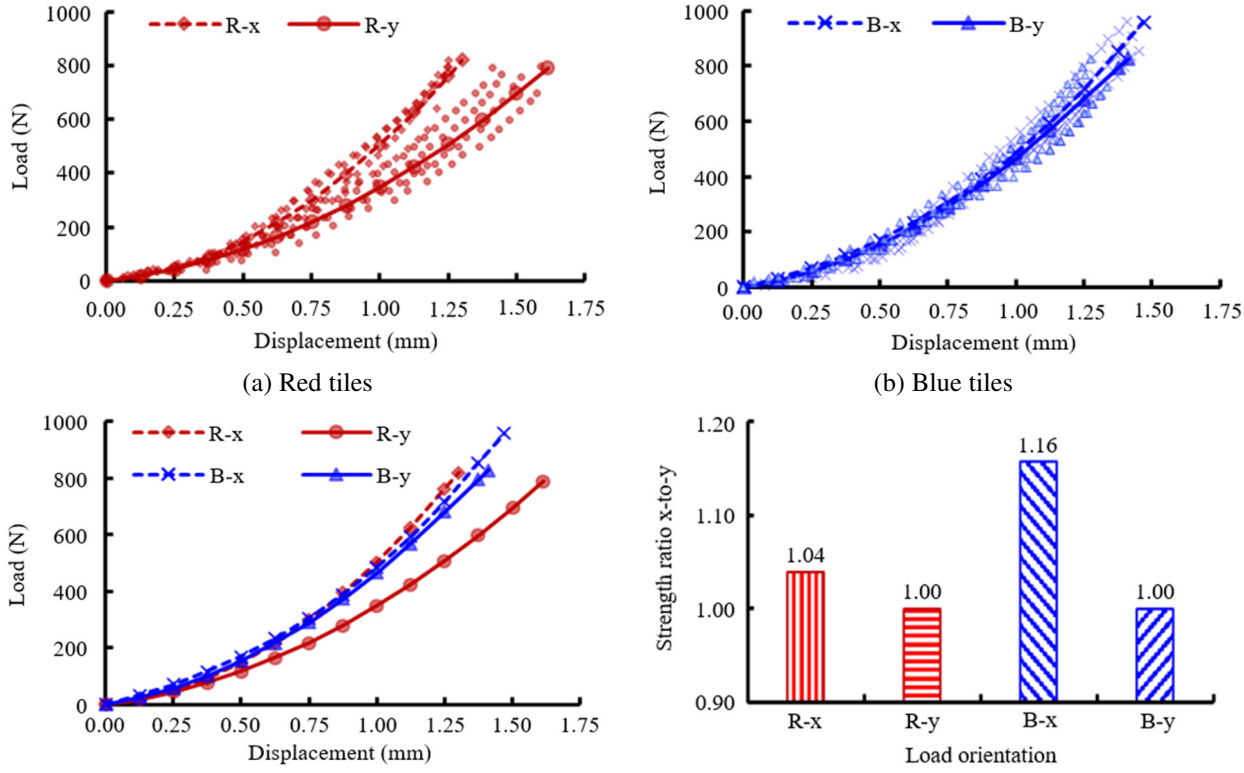

(a) Red tiles (b) Blue tiles

(c) Behavior comparison (d) Ultimate load ratio

Fig. 8 Load-displacement behavior

The ultimate displacement is generally uniform and fluctuates from 1.3 to 1.6 mm, depending on the load orientation. The *x*-axis direction was less ductile because of the larger section's moment of inertia. Corresponding to these findings, the initial stiffness of specimens was obtained. The results showed that the initial stiffness of the *x*-axis loading direction always exceeds the *y*-axis direction. The absorption rate of the blue tiles surpassed the red tiles by 47.5%. Since the uncoated tile absorption is a constant, the differentiation originates from the characteristics of the coating. The failure mode was distinctively flexure. Due to its brittle nature, initial cracking is visually unobservable. In contrast, however, the FE model provided valuable input on this subject. The tiles had a plane failure surface in the line of loading, located at the maximum bending moment (Fig. 9). No shear cracks were detected, and the tile material in the compression area was undisturbed. The presence of the coating shifted the neutral axes to the top fibers, reducing the strain in the compressive zone.

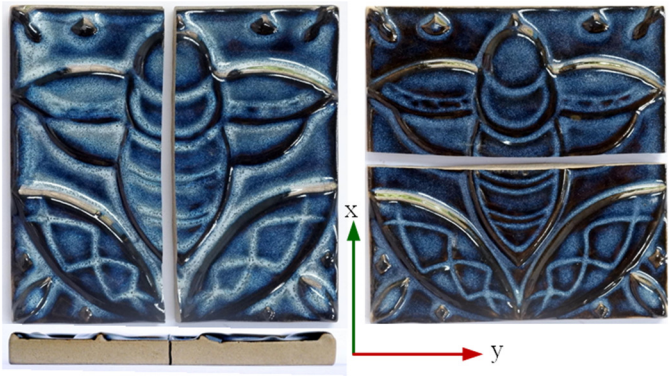

Fig. 9 Failure mode

4.2. FE model validation and result

The FE model was subjected to a sensitivity analysis, concerning meshing techniques and element finesses, to obtain a convergent load state, as shown in Fig. 10. In the sensitivity analysis, different sizes of elements were employed for the B_x specimens under examination, including 1.0 mm, 1.5 mm, 2.0 mm, and 2.5 mm, resulting in a varying number of total elements: 234,094, 72,154, 32,064, and 14,964, respectively. To achieve a compromise between factors such as failure patterns, analysis times, and the degree of agreement with experimental and computational stability, a mesh size of 1.5 mm was selected for this study.

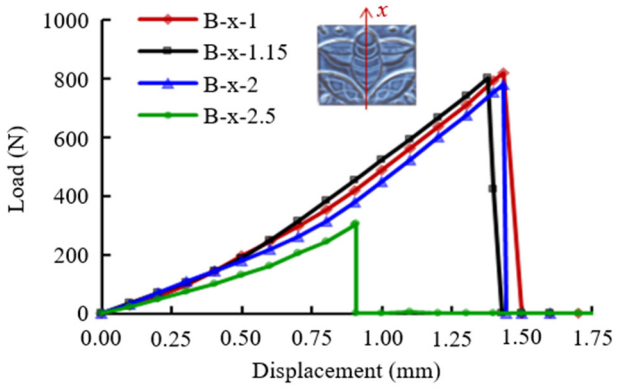

Fig. 10 Mesh sensitivity analysis

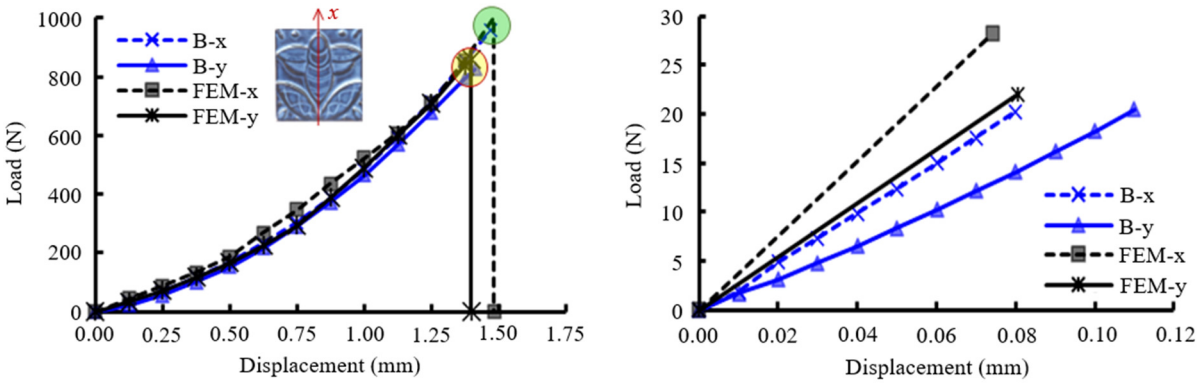

(a) FE model validation to experimental data (b) Initial stiffness observations

Fig. 11 Validation of FE model output

The load-displacement responses were generated for the blue tiles in both the *x* and *y*-axis directions. Fig. 11(a) presents the validation between the experimental and numerical model data. The model was in decent agreement with the experimental response. The ultimate load in both the *x* and *y* directions, the nonlinear load-displacement response, and the ultimate displacements were predicted with high accuracy. To evaluate the initial stiffness at first cracking, Fig. 11(b) was generated.

The response was linear, underlining that nonlinearity was a result of crack propagation and stress redistribution. The loading orientation from the *x* to the *y* axes reduces the stiffness by 6%. The analyses demonstrated that the bee design with a higher moment of inertia contributed to a larger section stiffness. The FE model overpredicted the initial stiffness for all cases. It was subsequently postulated that, in the FE model, all elements except the components of the model, the rubber bearing, and the rods were perfectly rigid. Furthermore, the presence of voids in the tile material was not considered in the analysis.

The FE model presented a sophisticated tool to analyze the behavior of 3D bee-crop-circle tiles under concentrated loading. The *x*-axis orientation was chosen for evaluation purposes since it resulted in the most distinguishing influence compared to the *y* direction.

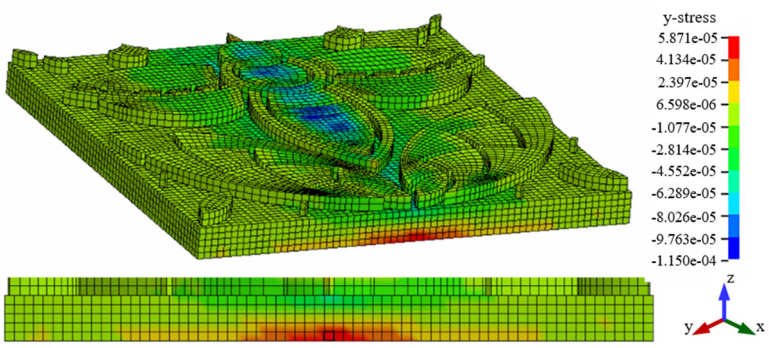

(a) Stress pattern

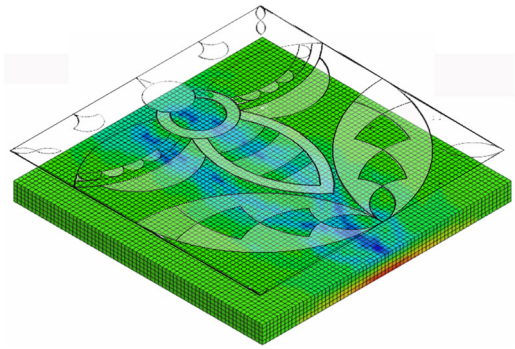

(b) Stress distribution under the relief

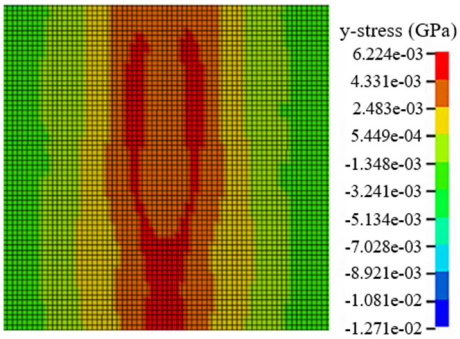

(c) Stress concentration before first cracking

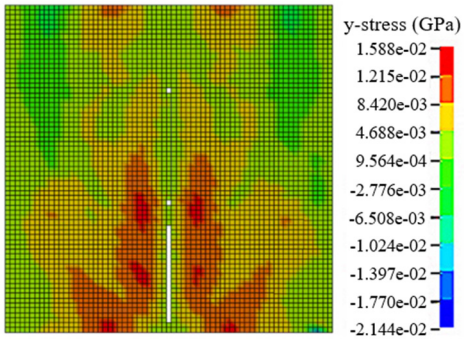

(d) First cracking and stress redistribution

Fig. 12 Stresses at first and ultimate cracking

The first cracking was detected in the line of loading, at the outermost fibers in tension (Fig. 12(a)). By observing the stress pattern beneath the bee relief (Fig. 12(b)), the areas directly under the boundaries of the bee induced the highest stress concentrations, and the arch-action within the bee's curved cross-section distributed the stresses to the outer perimeters of the bee. Before the failure, the stress pattern beneath the bee showed a clear impact of the arc-formed bee on the stress distribution (Fig 12(c)): the stresses at the arc-end measured 6.22 MPa, compared to 2.43 MPa under the bee. Fig 12(d) shows the first cracking in the elements, as seen from the bottom fibers of the tile and stress redistribution. The stress at failure in this element was recorded as 10.86 MPa, exceeding the 10.71 MPa modulus of rupture. The strain was recorded to be 0.000552 mm/mm.

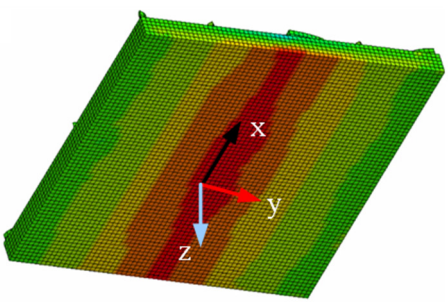

(a) Stresses underneath the tile

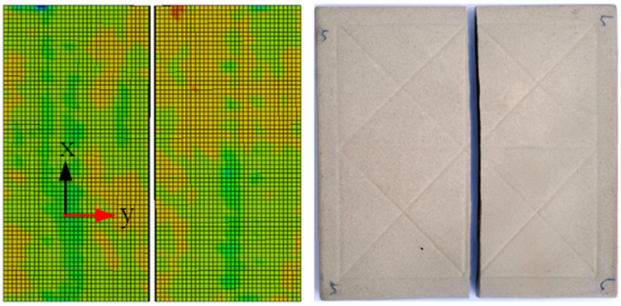

(b) FE model crack simulation and real tile

Fig. 13 FE model - final stages

In the final stages, the stresses in the outer bottom tensile fibers propagated along the *x*-axes (as seen in Fig. 13(a)), resulting in the cracking of the tile (Fig. 13(b)). This pattern confirms the failure mode observed from the experimentally tested specimens. The FE model enabled it to analyze the complexity of the design, resulting in a two-dimensional loading scheme in combination with a 3D stress response.

5. Conclusion

The 3D bee-crop-circle tile design resulted in a complex stress distribution behavior due to the amalgamation of a variation with inertia along the plane of loading. The presence of curved formations in the line of loading, due to the bee's body, resulted in an arch-action. Loads applied on an arch are distributed tangential to the curve, resulting in one force vector along the body, and one perpendicular to the arch. Following the mechanics of an arch, this load vector created lower stresses, compared to the same load magnitude applied to a flat element. The ends of the arch function as arch supports, creating larger stresses in this region compared with the regions beneath the arch. Eventually, the failure mode was determined by the location of the maximum flexural stresses in the line of loading. Some findings are elaborated as follows:

(1) The *h*-refinement followed by an optimization of meshing finesses should be conducted, while the loading increment should exactly resemble the actual loading sequences in the laboratory.

(2) The crop design significantly influences the load-carrying capacity of the tiles due to the variations in thickness and the presence of curved formations that alter the load distribution on the tile itself.

(3) The coloring technique also affects the load capacity and is mostly a function of the coating type and thickness of the painting layer.

(4) It is recommended that a detailed numerical model is run before proceeding to the further mass production of tiles.

Acknowledgment

The authors acknowledge the support provided by the Directorate of Research and Innovation Funding, National Research and Innovation Agency, and LPDP - Ministry of Finance, under RIIM Research Grant 2022 (Contract No. 947-08/UN7.D2/KS/XI/2022). Additionally, appreciation is extended to Universitas Diponegoro and PT Gyan Kreatif, Indonesia, for their contribution to this work.

Nomenclature or Abbreviations

3D	Three-dimensional	SSD	Single shot multibox detector
A, B, C, M, N	Material constants	t	The thickness of the ceramics tile (mm)
C_{01}, C_{10}	Material constants	T	The maximum tensile hydrostatic pressure
D	The damage ($0 < D \leq 1.0$)	T^*	The normalized maximum tensile hydrostatic pressure
D_1, D_2	Constants	W	The first-order Mooney-Rivlin hyperelastic material's strain energy
E	Elastic modulus	x	*x*-direction
E	The Green–St. Venant strain tensor	y	*y*-direction
EPSI	Reference strain rate	YOLOv3	The You Only Look Once method version 3
FE	Finite element	z	z-direction
FEM	Finite element model	σ^*	The normalized equivalent stress
FS	Failure strain	σ_i^*	The normalized intact equivalent stress
G	Shear modulus	σ_f^*	The normalized fracture stress
HEL	Hugoniot elastic limit	σ_{HEL}	The equivalent stress at the HEL

IRHD	International rubber hardness degree	$\Delta\epsilon_p$	The increase in plastic strain
ISO	International organization for standardization	ϵ^*	The dimensionless strain rate
JH	Johnson-Holmquist	ϵ_p^f	The plastic strain at fracture
K	Bulk modulus	ϵ_{11}	The one-dimensional strain component of Green-St. Venant
K_1, K_2, K_3	Material constants (K_1 is bulk modulus)	μ	The material deformation
L	Length of the ceramic tile	ρ	The current density
LVDT	Linear variable differential transformer	ρ_0	The initial density
P	The current pressure	ν	Poisson's ratio
P^*	The normalized pressure	λ	Stretch
P_{HEL}	The pressure at the HEL	λ_1	Principal stretch
ΔP	The additional incremental pressure		

Conflicts of Interest

The authors declare no conflict of interest.

References

[1] Kartono, R. H. S. Utomo, S. S. Priyo, and T. S. Ujiani, "Crystallographic Tile," Journal of Physics: Conference Series, vol. 1025, article no. 012087, 2018.

[2] Kartono, R. H. S. Utomo, P. S. Sasongko, and T. Udjiani, "Application of the Crystallographic Tiling to Increase Competitiveness of the Sand Sediments," Journal of Physics: Conference Series, vol. 1217, article no. 012062, 2019.

[3] M. Nur, "Menguak Misteri Crop Circle Di Indonesia," 1st ed., Yogyakarta: Graha Ilmu, 2011. (In Bahasa Indonesia)

[4] P. W. Anggoro, T. Yuniarto, B. Bawono1, D. B. Setyohadi, S. Felasari, O. D. W. Widyanarka, et al., "Advanced Design and Fabrication of Islamic Tile Ceramic Wall Tiles with Indonesian Batik Patterns Using Artistic CAD/CAM and 3D Printing Technology," Frontiers in Mechanical Engineering, vol. 7, article no. 799086, February 2022.

[5] C. T. Brasileiro, S. Conte, F. Contartesi, F. G. Melchiades, C. Zanelli, M. Dondi, et al., "Effect of Strong Mineral Fluxes on Sintering of Porcelain Stoneware Tiles," Journal of the European Ceramic Society, vol. 41, no. 11, pp. 5755-5767, September 2021.

[6] K. Wiśniewska, W. Pichór, and E. Kłosek-Wawrzyn, "Influence of Firing Temperature on Phase Composition and Color Properties of Ceramic Tile Bodies," Materials, vol. 14, no. 21, article no. 6380, November 2021.

[7] O. Abiola, A. Oke, B. Omidiji, and D. Adetan, "Effect of Firing Temperature on Some Mechanical Properties of Osun State Ceramic Tiles," East African Journal of Engineering, vol. 4, no. 1, pp. 13-21, October 2022.

[8] I. C. Bernardo-Arugay, F. J. A. Echavez, R. H. L. Aquiatan, C. B. Tabelin, R. V. R. Virtudazo, and V. J. T. Resabal, "Development of Ceramic Tiles from Philippine Nickel Laterite Mine Waste by Ceramic Casting Method," Minerals, vol. 12, no. 5, article no. 579, May 2022.

[9] T. Húlan, I. Štubňa, J. Ondruška, and A. Trník, "The Influence of Fly Ash on Mechanical Properties of Clay-Based Ceramics," Minerals, vol. 10, no. 10, article no. 930, October 2020.

[10] K. K. Thakur, M. M. Shafeeq, A. Rahman, and D. P. Mondal, "Effect of Sintering Temperature and Binder Addition on the Properties of Cupola Slag Glass–Ceramic Tiles," International Journal of Environmental Science and Technology, vol. 19, no. 11, pp. 11387-11396, November 2022.

[11] K. Schabowicz, "Testing of Materials and Elements in Civil Engineering," Materials, vol. 14, no. 12, article no. 3412, June 2021.

[12] H. Zhang, L. Peng, S. Yu, and W. Qu, "Detection of Surface Defects in Ceramic Tiles with Complex Texture," IEEE Access, vol. 9, pp. 92788-92797, June 2021.

[13] Z. Zhao, "Review of Non-Destructive Testing Methods for Defect Detection of Ceramics," Ceramics International, vol. 47, no. 4, pp. 4389-4397, February 2021.

[14] Q. Lu, J. Lin, L. Luo, Y. Zhang, and W. Zhu, "A Supervised Approach for Automated Surface Defect Detection in Ceramic Tile Quality Control," Advanced Engineering Informatics, vol. 53, article no. 101692, August 2022.

[15] G. Wan, H. Fang, D. Wang, J. Yan, and B. Xie, "Ceramic Tile Surface Defect Detection Based on Deep Learning," Ceramics International, vol. 48, no. 8, pp. 11085-11093, April 2022.
[16] B. N. de Souza, M. Dal Bó, D. Hotza, and M. C. Fredel, "Chemical Modification of Porcelain Tile Surface to Optimize Flexural Strength and Weibull Modulus Through the Ion Exchange Process," Journal of Building Engineering, vol. 56, article no. 104735, September 2022.
[17] M. E. Mahmoud, A. M. El-Khatib, A. M. Halbas, and R. M. El-Sharkawy, "Investigation of Physical, Mechanical and Gamma-Ray Shielding Properties Using Ceramic Tiles Incorporated with Powdered Lead Oxide," Ceramics International, vol. 46, no. 10, Part A, pp. 15686-15694, July 2020.
[18] K. Ałykow, Ł. Bednarz, M. Piechówka-Mielnik, M. Napiórkowska-Ałykow, and M. Krupa, "New Ceramic Tiles Produced Using Old Technology Applied on Historic Roofs—Possibilities and Challenges," Materials, vol. 15, no. 21, article no. 7835, November 2022.
[19] S. Alraddadi and H. Assaedi, "Thermal and Mechanical Properties of Glass–Ceramics Based on Slate and Natural Raw Materials," Silicon, vol. 15, no. 4, pp. 1871-1882, February 2023.
[20] W. Xu, K. Li, Y. Li, Y. Sun, Y. Bao, D. Wan, et al., "Surface Strengthening of Building Tiles by Ion Exchange with Adding Molten Salt of KOH," International Journal of Applied Ceramic Technology, vol. 19, no. 3, pp. 1490-1497, May/June 2022.
[21] J. Wu, K. Tian, C. Wu, J. Yu, H. Wang, J. Song, et al., "Effect of Talc on Microstructure and Properties of the Graphite Tailing Stoneware Tiles," Construction and Building Materials, vol. 311, article no. 125314, December 2021.
[22] P. de Oliveira Piccolo, A. Zaccaron, L. B. Teixeira, E. G. de Moraes, O. R. K. Montedo, and A. P. N. de Oliveira, "Development of Translucent Ceramic Tiles from Modified Porcelain Stoneware Tile Paste," Journal of Building Engineering, vol. 45, article no. 103543, January 2022.
[23] C. Molinari, Y. Alaya, L. Pasti, G. Guarini, M. Dondi, and C. Zanelli, "Assessing White Clays from Tabarka (Tunisia) in the Production of Porcelain Stoneware Tiles," Applied Clay Science, vol. 231, article no. 106741, January 2023.
[24] T. Yibing, "Technical Analysis of Water Absorption Rate of Ceramic Tiles," E3S Web of Conferences, vol. 185, article no. 04039, 2020.
[25] G. R. Johnson and T. J. Holmquist, "An Improved Computational Constitutive Model for Brittle Materials," AIP Conference Proceedings, vol. 309, no. 1, pp. 981-984, July 1994.
[26] D. S. Cronin, K. Bui, C. Kaufmann, G. Mcintosh, and T. Berstad, "Implementation and Validation of the Johnson-Holmquist Ceramic Material Model in LS-Dyna," 4th European LS-DYNA Users Conference, pp. 47-60, May 2003.
[27] A. Ruggiero, G. Iannitti, N. Bonora, and M. Ferraro, "Determination of Johnson-Holmquist Constitutive Model Parameters for Fused Silica," EPJ Web of Conferences, article no. 04011, 2012.
[28] A. J. Flynn and Z. H. Stachurski, "Microstructure and Properties of Stoneware Clay Bodies," Clay Minerals, vol. 41, no. 3, pp. 775-789, September 2006.
[29] G. Tuomas, "Water Powered Percussive Rock Drilling: Process Analysis, Modelling and Numerical Simulation," Ph.D. dissertation, Department of Civil and Environmental Engineering, Luleå University of Technology, Luleå, Sweden, 2004.
[30] S. J. Jerrams and J. Bowen, "Modelling the Behaviour of Rubber-Like Materials to Obtain Correlation with Rigidity Modulus Tests," WIT Transactions on Modelling and Simulation, vol. 12, pp. 511-518, 1995.